





# Manipulation of spin orientation via ferroelectric switching in Fe-doped $\text{Bi}_2\text{WO}_6$ from first principles

Katherine Inzani <sup>1,2,3</sup>, Nabaraj Pokhrel <sup>4</sup>, Nima Leclerc <sup>2,5</sup>, Zachary Clemens <sup>6</sup>, Sriram P. Ramkumar <sup>6</sup>, Sinéad M. Griffin,<sup>1,2</sup> and Elizabeth A. Nowadnick<sup>6</sup>

<sup>1</sup>Materials Science Division, Lawrence Berkeley National Laboratory, Berkeley, California 94720, USA

<sup>2</sup>Molecular Foundry, Lawrence Berkeley National Laboratory, Berkeley, California 94720, USA

<sup>3</sup>School of Chemistry, University of Nottingham, Nottingham, NG7 2RD, United Kingdom

<sup>4</sup>Department of Physics, University of California, Merced, California 95343, USA

<sup>5</sup>Department of Electrical and Systems Engineering, University of Pennsylvania, Philadelphia, Pennsylvania 19104, USA

<sup>6</sup>Department of Materials Science and Engineering, University of California, Merced, California 95343, USA



(Received 7 December 2021; accepted 9 February 2022; published 28 February 2022)

Atomic-scale control of spins by electric fields is highly desirable for future technological applications. Magnetically doped Aurivillius-phase oxides present one route to achieve this, with magnetic ions substituted into the ferroelectric structure at dilute concentrations, resulting in spin-charge coupling. However, there has been minimal exploration of the ferroelectric switching pathways in this materials class, limiting predictions of the influence of an electric field on magnetic spins in the structure. Here, we determine the ferroelectric switching pathways of the end member of the Aurivillius phase family,  $\text{Bi}_2\text{WO}_6$ , using a combination of group theoretic analysis and density functional theory calculations. We find that in the ground state  $P2_1ab$  phase, a two-step switching pathway via  $C2$  and  $Cm$  intermediate phases provides the lowest energy barrier. Considering iron substitutions on the W site in  $\text{Bi}_2\text{WO}_6$ , we determine the spin easy axis. By tracking the change in spin directionality during ferroelectric switching, we find that a  $90^\circ$  switch in the polarization direction leads to a  $112^\circ$  reorientation of the spin easy axis. The low-symmetry crystal-field environment of  $\text{Bi}_2\text{WO}_6$  and magnetoelastic coupling on the magnetic dopant provide a route to spin control via an applied electric field.

DOI: [10.1103/PhysRevB.105.054434](https://doi.org/10.1103/PhysRevB.105.054434)

## I. INTRODUCTION

Multiferroic materials with coupled ferroic orderings (e.g., ferromagnetism, ferroelectricity, and ferroelasticity) exhibit intriguing physics and hold potential for enabling new types of future electronic devices [1]. In magnetoelectric materials with coupled ferroelectricity and magnetism, the ability to switch the magnetization by an applied electric field is particularly promising for low-power spintronics [2]. Materials approaches to multiferroicity, for example, multiferroic superlattices [3], nanocomposites [4], domain walls [5], and single phase materials [6], typically focus on realizing long-range magnetic order for macroscopic devices. However, several recent works have pushed toward the fundamental limits of multiferroic phenomena, including electric field manipulation of molecular magnets [7,8], tuning exchange in a molecular system [9], and the coherent electric field control of dilute iron dopants in a ferroelectric crystal [10]. These milestones toward full control of isolated spins by electric fields may enable new functionalities in classical electronic devices in the field of spintronics as well as in quantum computing [10,11].

A promising pathway to achieve isolated spin centers with magnetoelectric coupling is to dope a ferroelectric structure with dilute concentrations of magnetic ions [10]. Here, magnetoelectricity arises by coupling the ferroelectric's polar distortion with the spin dopant through spin-orbit interactions.

This approach confers the rich phase space of ferroelectric crystals, in particular, of complex oxide materials, for use as hosts for spin dopants. In particular, the versatile structural motifs and distortions in ferroelectric oxides provide a highly tunable local environment for the spin center, allowing control of the magnetocrystalline properties via the crystal field environment. The symmetry lowering caused by the ferroelectric distortion results in magnetocrystalline anisotropies that lead to preferential alignment of spins within a plane (spin easy plane) or along an axis (spin easy axis). Using the prototypical ferroelectric  $\text{PbTiO}_3$  as a host for  $\text{Fe}^{3+}$  spins, some of the present authors recently demonstrated that the tetragonal polar distortion results in a spin easy plane with  $90^\circ$  switching under the application of an electric field [10]. However, preferentially aligning spins along an easy axis and  $180^\circ$  switching would have technical advantages for applications. Ferroelectric hosts providing lower crystallographic symmetries in the vicinity of the spin are more likely to support spin easy axes due to their highly distorted crystal fields, and so are sought for such ferroelectric-mediated spin switching.

The Aurivillius phases are a family of layered ferroelectric materials with low-symmetry crystal structures that could satisfy these requirements. The Aurivillius structure is composed of  $m$  perovskitelike layers  $(A_{m-1}B_mO_{3m+1})^{2-}$  interspersed with fluoritelike  $(\text{Bi}_2\text{O}_2)^{2+}$  layers, giving the overall general

formula  $\text{Bi}_2A_{m-1}B_m\text{O}_{3m+3}$ . The Aurivillius phases are well known for their robust ferroelectricity, including high Curie temperatures ( $T_C$ ), large spontaneous polarizations [12–14], and fatigue resistance [15]. Furthermore, the composition has great versatility owing to the different cations that can be placed on the  $A$  and  $B$  sites, which has led to efforts to design multiferroic Aurivillius compounds via incorporation of magnetic ions [16–22]. Most work has focused on achieving long-range magnetic ordering in single-phase materials with large proportions of magnetic cations, for example, in doped  $\text{Bi}_{n+1}\text{Fe}_{n-3}\text{Ti}_3\text{O}_{3n+3}$  compounds. However, the complex crystal structure and difficulty in synthesis of phase pure samples has made characterization of the multiferroic properties difficult [21,23,24]. In particular, the ferroelectric and magnetoelectric switching mechanisms have not been elucidated [25]. These limitations hinder the prediction of the behavior of magnetic spins during switching. Moreover, to the best of our knowledge, magnetoelectric coupling of isolated magnetic dopants has not yet been investigated in this class of materials.

Here, we use group theoretic analysis and first-principles calculations to explore ferroelectric switching and control of magnetic dopants in the end member of the Aurivillius family,  $\text{Bi}_2\text{WO}_6$  ( $m=1$ ,  $B=W$ ). We select  $\text{Bi}_2\text{WO}_6$  because it exhibits robust ferroelectricity and also possesses a complex crystal structure which can provide a low-symmetry crystallographic environment for magnetic dopants. Theoretical and experimental work has revealed that ferroelectricity in  $\text{Bi}_2\text{WO}_6$  arises from an instability to a polar distortion involving large Bi displacements with respect to the perovskite layer [26–30]. It undergoes a two-step paraelectric-ferroelectric phase transition sequence: at room temperature,  $\text{Bi}_2\text{WO}_6$  crystallizes in the orthorhombic ferroelectric phase  $P2_1ab$ , then transitions to the polar orthorhombic structure  $B2cb$  at 670 °C, and finally transitions to the paraelectric monoclinic phase  $A2/m$  above 950 °C [31].

Experiments have reported that ferroelectric switching in  $\text{Bi}_2\text{WO}_6$  proceeds via a two-step process [29], but the details of the precise switching pathway taken are still lacking. We therefore start by determining the likely ferroelectric switching pathway by systematically enumerating and then evaluating the energetics of several possible symmetry-distinct paths. Here we consider *intrinsic* ferroelectric switching paths, where we calculate energy barriers for coherent polarization reversal in a single infinite domain [32]. Although this does not provide a full description of the dynamic ferroelectric switching process, work on other ferroelectrics [33,34] has shown that when multiple symmetry-distinct switching paths are available, intrinsic barriers can correctly identify the experimental switching path. We then introduce  $\text{Fe}^{3+}$  dopants into the structure at dilute concentrations and track the change in spin directionality with ferroelectric switching. This paper lends understanding to the magnetoelectric effects on isolated spins in  $\text{Bi}_2\text{WO}_6$ , demonstrating the potential for atomic-scale spin control in the Aurivillius class of materials.

## II. COMPUTATIONAL METHODOLOGY

We perform density functional theory (DFT) calculations using the VIENNA AB INITIO SIMULATION PACKAGE (VASP)

[35–38], using projector augmented-wave pseudopotentials [39,40] including  $\text{Bi } 5d^{10}6s^26p^3$ ,  $\text{W } 5p^65d^46s^2$ ,  $\text{O } 2s^22p^4$ , and  $\text{Fe } 3d^64s^2$  as valence electrons. A plane-wave cut-off energy of 800 eV is used with a  $6 \times 6 \times 2$   $\Gamma$ -centered  $k$ -point grid (for the  $P2_1ab$   $\text{Bi}_2\text{WO}_6$  36-atom unit cell), which converges the total energy to 1 meV per formula unit (f.u.). The same  $k$ -point grid is used for all undoped structures, and a  $2 \times 2 \times 2$   $k$ -point grid is used for the doped supercells. All calculations are done using the generalized gradient approximation-based exchange-correlation functional PBEsol [41], which gives lattice parameters within 1% of experiment [30] ( $a = 5.443 \text{ \AA}$ ,  $b = 5.443 \text{ \AA}$ ,  $c = 16.557 \text{ \AA}$  for  $P2_1ab$ ).

For undoped structures, we allow the ionic positions, cell volume, and cell shape to optimize and apply a force tolerance convergence of  $1 \text{ meV \AA}^{-1}$ . The nudged elastic band (NEB) method [42] implemented in VASP is employed to find the structural parameters and energies of intermediate structures lying along the ferroelectric switching pathways. For the NEB calculations, the force convergence tolerance is increased to  $10 \text{ meV \AA}^{-1}$ .

We include  $\text{Fe}^{3+}$  substitutional defects on W sites in  $2 \times 2 \times 1$  supercells of  $\text{Bi}_2\text{WO}_6$  (144 atoms), with three electrons added for charge compensation. For structures containing more than one symmetrically inequivalent W site, we consider each as a different dopant site. An effective Hubbard term  $U_{\text{eff}} = U - J = 4 \text{ eV}$  is added to the Fe  $d$  orbitals within the Dudarev approach [43]. Geometry optimization of the ions for each defect supercell is completed to a force convergence of  $10 \text{ meV \AA}^{-1}$ , while keeping the cell volume and shape fixed. Magnetocrystalline anisotropy energy (MCAE) surfaces are calculated by including spin-orbit coupling self-consistently and varying the spin quantization axes over 194 points. We make use of the ISOTROPY software suite [44] for group theoretic analysis and VESTA [45] for the visualization of crystal structures.

## III. RESULTS AND DISCUSSION

### A. Ground-state crystal structure

To set the stage for understanding ferroelectric switching, we first analyze the structural distortions present in the ferroelectric  $P2_1ab$  structure. The  $P2_1ab$  space group is established by the condensation of three distinct structural distortions that transform like irreducible representations (irreps) of the high-symmetry reference structure  $I4/mmm$  [Figs. 1(a) and 1(b)]. These distortions are a polar displacement along the  $[1\ 0\ 0]$  orthorhombic axis which transforms like the irrep  $\Gamma_5^-$ , an octahedral rotation about  $[0\ 0\ 1]$  which transforms like  $X_2^+$ , and an out-of-phase ( $a^-a^-c^0$  in Glazer notation [46]) octahedral tilt about  $[1\ 0\ 0]$  which transforms like  $X_3^+$  [Figs. 1(c)–1(e)]. The amplitudes of these three distortions, computed from DFT-relaxed and experimental structures, are reported in Table I. Overall, the distortion amplitudes show good agreement between DFT and experiments. The main contribution to the polar distortion comes from displacement of the Bi cations against the O2 atoms as shown in Fig. 1(c). In addition to the three distortions discussed above, there are several other distortions which are symmetry allowed in the  $P2_1ab$  structure, but they have

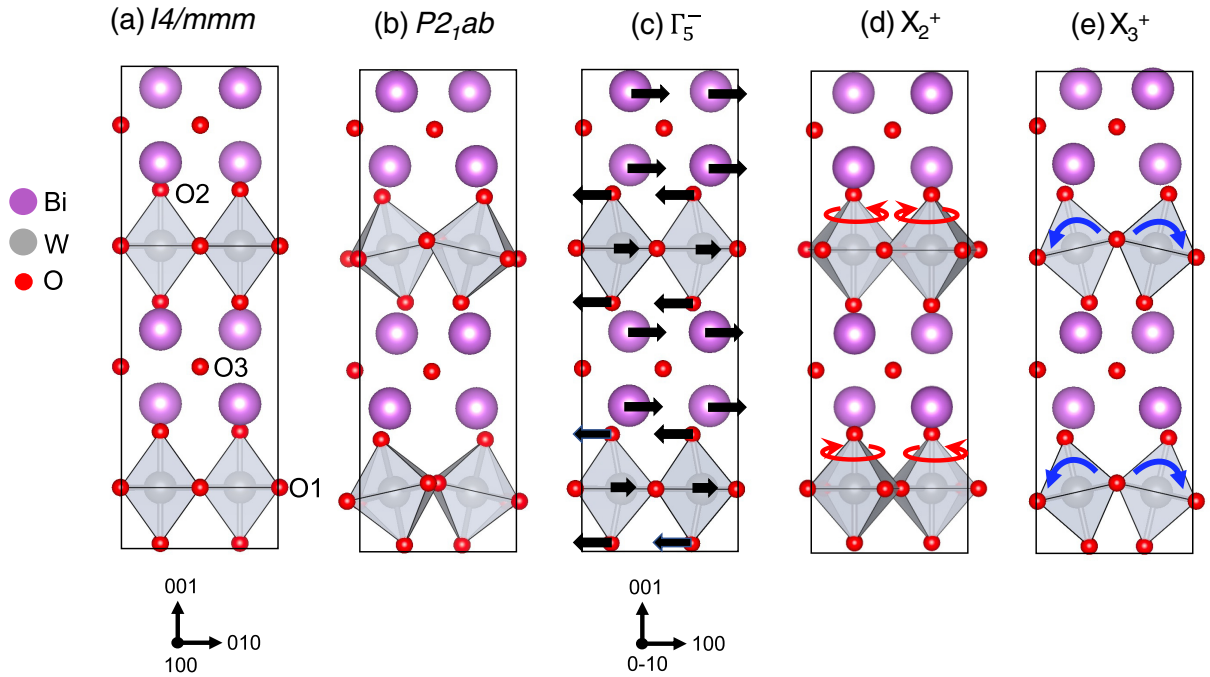


FIG. 1. The (a) high-symmetry reference structure  $I4/mmm$  and (b) polar orthorhombic structure  $P2_1ab$  of  $\text{Bi}_2\text{WO}_6$ . A structural decomposition of  $P2_1ab$  into symmetry-adapted modes of  $I4/mmm$  reveals three main structural distortions: (c) a polar displacement along  $[1\ 0\ 0]$  with symmetry  $\Gamma_5^-$ , (d) an octahedral rotation about  $[0\ 0\ 1]$  with symmetry  $X_2^+$ , and (e) an out-of-phase octahedral tilt about  $[1\ 0\ 0]$  with symmetry  $X_3^+$ . The axes shown under panel (a) are used for all panels except for (c).

negligible amplitudes [28] so we do not consider them in this paper.

### B. Ferroelectric switching pathways

To provide a framework for systematically identifying ferroelectric switching pathways, we next enumerate possible metastable structural phases of  $\text{Bi}_2\text{WO}_6$  and compute their energies with DFT. The key to uncovering the metastable structural phases is to recognize that each of the three structural distortions shown in Fig. 1 is described by a two-dimensional order parameter  $Qe^{i\alpha}$  [34]. Here  $Q$  is the order

TABLE I. Decomposition of the  $\text{Bi}_2\text{WO}_6$   $P2_1ab$  structure (DFT relaxed and experimental) into symmetry-adapted modes of  $I4/mmm$ . The experimental structure is taken from Ref. [47]. The amplitudes are given in Å for a 36-atom cell. For the O1 atoms, the coordinates in parentheses indicate the axes along which the atoms displace; there are two distinct O1 displacement patterns in the  $xy$  plane that are consistent with the symmetry.

Atom	$\Gamma_5^-$		$X_2^+$		$X_3^+$	
	DFT	Expt.	DFT	Expt.	DFT	Expt.
Bi	0.66	0.68	0	0	0.33	0.30
W	0.18	0.25	0	0	0	0
O1(z)	0	0	0	0	0.87	0.70
O1(xy)	-0.15	-0.11	0.75	0.85	0	0
O1(xy)	-0.25	-0.29	-0.01	-0.02	0	0
O2	-0.77	-0.74	0	0	-1.10	-0.89
O3	0.27	0.17	0	0	-0.05	-0.02
Total	1.10	1.09	0.75	0.85	1.44	1.17

parameter amplitude and  $\alpha$  is the phase. For the  $X_3^+$  octahedral tilt and the  $\Gamma_5^-$  polar distortion, the phase  $\alpha$  describes the orientation of the tilt (polar) axis. For the  $X_2^+$  octahedral rotation, the phase describes the relative sense of the octahedral rotations in adjacent perovskite layers.

Each two-dimensional structural order parameter can lie along three symmetry-distinct directions  $(Q \cos \alpha, Q \sin \alpha) = (a, 0)$ ,  $(a, a)$ , or  $(a, b)$ , where  $a \neq b$  are real numbers and each direction establishes a different subgroup of  $I4/mmm$ . For example, the  $P2_1ab$  space group is established by condensing the  $X_3^+$ ,  $X_2^+$ , and  $\Gamma_5^-$  distortions along the  $(0, a)$ ,  $(a, 0)$ , and  $(a, a)$  order parameter directions, respectively. Taking these order parameters to lie along different combinations of directions generates structures of different symmetries. In Table II, we consider all other possible combinations of the  $X_3^+$ ,  $X_2^+$ , and  $\Gamma_5^-$  order parameter directions, and enumerate the space groups that these generate (we do not include the low-symmetry  $(a, b)$  direction in this enumeration because structures defined by this direction generally return to a higher symmetry direction upon DFT relaxation). Table II also shows space groups that are generated by combining two out of the three order parameters taken along different combinations of directions. Space groups generated by each order parameter individually are given in Appendix A.

We then perform structural relaxations of  $\text{Bi}_2\text{WO}_6$  with its symmetry constrained to each space group identified in Table II, and report the resulting energy and structural parameters. Most metastable structures have energies ranging from  $\approx 65$  to  $\approx 160$  meV per f.u. above  $P2_1ab$ . We find two very low energy structures:  $B2cb$  (4.38 meV/f.u.) and  $Pc$ , which we find to be slightly lower in energy than  $P2_1ab$ .

TABLE II. Subgroups of  $I4/mmm$  established by different combinations of the  $X_3^+$ ,  $X_2^+$ , and  $\Gamma_5^-$  order parameter directions. Total energies, distortion amplitudes, and lattice parameters obtained from DFT structural relaxations of  $\text{Bi}_2\text{WO}_6$  in each space group are given. The energies are reported relative to the energy of  $P2_1ab$ , which is set to 0 meV/f.u. If a structure relaxes to a higher symmetry space group, that space group is indicated in the energy column. The distortion amplitudes are obtained by decomposing the distorted structures with respect to  $I4/mmm$  and are reported for a 36-atom computational cell.

Irreps	Order parameter direction			Space group (N <sup>o</sup> )	Amplitude (Å)			Lattice parameters (Å)			Energy (meV/f.u.)
	$\Gamma_5^-$	$X_2^+$	$X_3^+$		$\Gamma_5^-$	$X_2^+$	$X_3^+$	$a$	$b$	$c$	
$X_2^+ \oplus X_3^+$		$(b, 0)$	$(c, 0)$	$I4/mmm$ (139)	0	0	0	3.806	3.806	16.453	355.51
		$(b, 0)$	$(0, c)$	$P2_1/c$ (14)	0	0.91	1.30	5.331	5.353	8.697	158.72
		$(b, 0)$	$(c, c)$	$Pcab$ (61)	0	0.78	1.35	5.350	5.360	16.844	149.74
		$(b, b)$	$(c, c)$	$C2/m$ (12)	0	0.48	1.46	7.602	7.614	16.602	157.40
$\Gamma_5^- \oplus X_3^+$	$(a, 0)$		$(c, c)$	$Cm2a$ (39)	0.44	0	1.53	7.601	7.754	16.481	103.46
	$(a, a)$		$(0, c)$	$B2cb$ (41)	1.19	0	1.60	5.467	5.472	16.553	4.38
	$(a, a)$		$(c, 0)$	$Bb2_1m$ (36)							$(Fmm2)$
$\Gamma_5^- \oplus X_2^+$	$(a, a)$	$(b, 0)$		$Bb2_1m$ (36)	0.98	1.24	0	5.389	5.395	16.481	67.05
	$(a, a)$	$(0, b)$		$Cm2a$ (39)	1.01	1.22	0	7.601	7.754	16.481	71.21
	$(a, 0)$	$(b, b)$		$Cm2m$ (38)	1.15	0.74	0	7.544	7.845	16.569	133.20
$\Gamma_5^- \oplus X_2^+ \oplus X_3^+$	$(0, a)$	$(b, b)$	$(c, c)$	$Cm$ (8)	0.45	0.53	1.46	7.729	7.584	16.506	99.06
	$(a, 0)$	$(b, b)$	$(c, c)$	$C2$ (5)	0.49	0.58	1.45	7.570	7.740	16.507	96.68
	$(a, a)$	$(b, 0)$	$(c, 0)$	$P2_1$ (4)							$(Bb2_1m)$
	$(a, a)$	$(0, b)$	$(0, c)$	$Pc$ (7)	1.11	0.76	1.44	5.442	5.443	8.688	-0.08
	$(a, a)$	$(b, 0)$	$(0, c)$	$P2_1ab$ (29)	1.11	0.75	1.44	5.443	5.443	16.557	0

The  $Pc$  and  $P2_1ab$  structures exhibit the same  $X_3^+$  and  $\Gamma_5^-$  distortions, the only difference is the relative sense of the  $X_2^+$  rotations in adjacent perovskite layers, thus it is unsurprising that these phases are very close in energy. We note that the relative energy of  $Pc$  and  $P2_1ab$  is quite sensitive to the value of the lattice parameters. For example, Ref. [28] found  $Pc$  to be about 3 meV/f.u. higher in energy than  $P2_1ab$  from DFT calculations with the LDA functional. Since  $P2_1ab$  is the experimentally reported ground state, we do not further consider the  $Pc$  phase here.

We next use the results of Table II to enumerate possible  $\text{Bi}_2\text{WO}_6$  ferroelectric switching pathways. The simplest way to reverse the polarization is in a single  $180^\circ$  step, where the polarization is brought to zero and then turned on again, pointing in the opposite direction, as shown in Fig. 2(a). At the midpoint of the path, the amplitude of the polarization is zero, and the symmetry of the crystal structure is  $Pcab$ , which is 149.74 meV/f.u. above the  $P2_1ab$  ground state structure (see Table II). The  $Pcab$  crystal structure is shown in Fig. 3(a).

In addition to the one-step  $Pcab$  switching path, we identify three two-step switching pathways, where the polarization reverses direction by rotating through two  $90^\circ$  steps (while maintaining finite amplitude). Since the  $\Gamma_5^-$  order parameter in  $P2_1ab$  is oriented along the  $(a, a)$  direction, rotating it by  $90^\circ$  takes it to either the  $(-a, a)$  or  $(a, -a)$  direction. This rotation requires that the  $\Gamma_5^-$  order parameter passes through the  $(0, a)$  or  $(a, 0)$  direction. Table II reveals that the  $Cm2a$ ,  $Cm2m$ ,  $C2$ , and  $Cm$  structures satisfy this requirement. Interestingly, the energies of  $Cm2a$ ,  $C2$ , and  $Cm$  are all near 100 meV/f.u. (within 10 meV/f.u. of each other), whereas  $Cm2m$  is somewhat higher (133.20 meV/f.u.). Due to its higher barrier, we do not consider the  $Cm2m$  pathway further in this paper.

Using these identified structures, we construct the two lowest energy two-step ferroelectric switching pathways in Figs. 2(b) and 2(c). Figure 2(b) shows a pathway that passes

through  $Cm2a$  twice as the polarization rotates in two  $90^\circ$  steps. At the midpoint of the switching path, the structure passes through an orthorhombic twin domain of  $P2_1ab$ . Note that the structure passes through different domains of  $Cm2a$  in

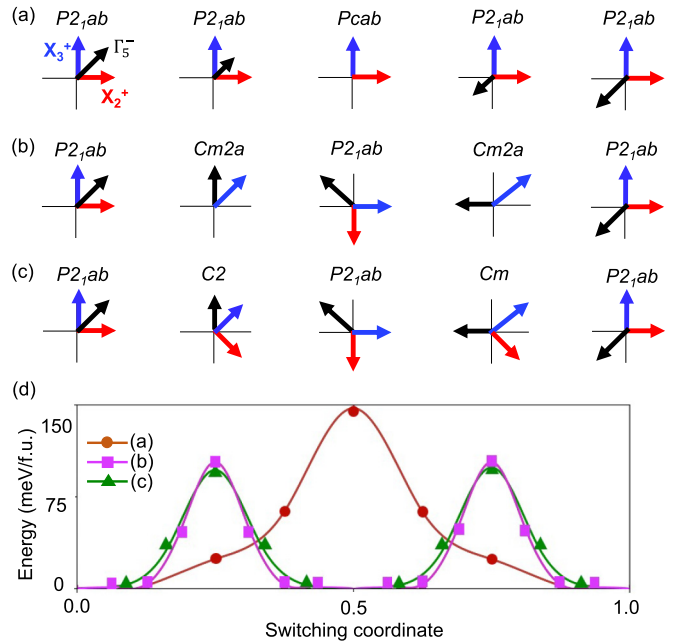


FIG. 2. Ferroelectric switching pathways in  $\text{Bi}_2\text{WO}_6$ . (a)–(c) show how the  $X_3^+$ ,  $X_2^+$ , and  $\Gamma_5^-$  order parameters, denoted by blue, red, and black arrows, respectively, evolve along the switching path. Path (a) is a one-step path, whereas paths (b) and (c) are two-step paths which pass through an orthorhombic twin of  $P2_1ab$  at the midpoint of the switching path. (d) Energy as a function of switching coordinate for the paths shown in (a)–(c).



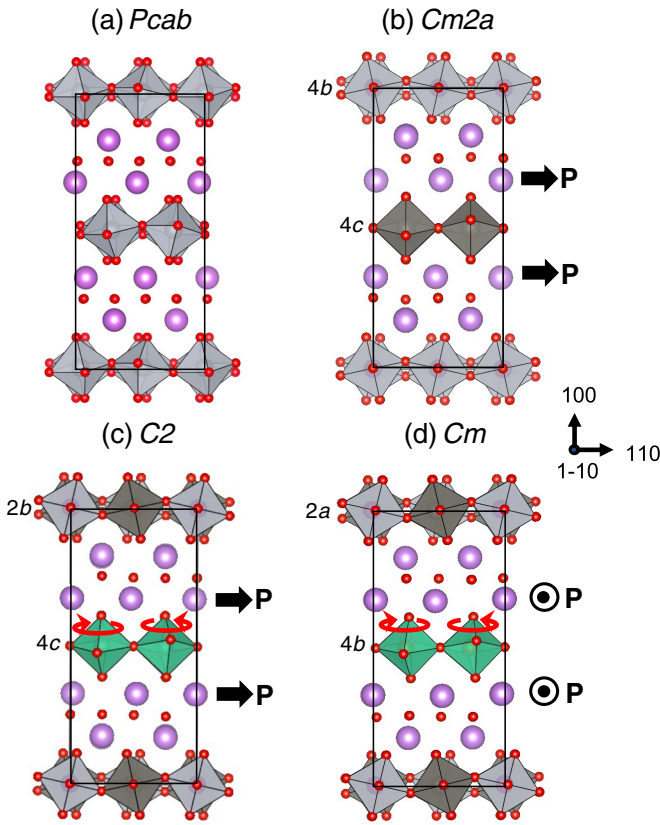


FIG. 3. Barrier structures of  $\text{Bi}_2\text{WO}_6$  realized along the ferroelectric switching paths. The  $Cm2a$  structure (b) has two distinct W Wyckoff positions, indicated by the light grey (4b) and dark grey (4c) octahedra. The  $C2$  structure (c) also has two distinct W Wyckoff positions, indicated by grey (2b) and green (4c) octahedra, and two symmetrically inequivalent W sites on the 2b position indicated in light and dark grey, respectively. Similarly, the  $Cm$  structure (d) has two distinct W Wyckoff positions, indicated by grey (2a) and green (4b) octahedra, and two symmetrically inequivalent W sites on the 2a position indicated in light and dark grey, respectively. The red arrows indicate the  $X_2^+$  rotations and the black arrows indicate the polarization direction.

the first and second steps. As the polarization rotates counterclockwise, the  $X_3^+$  order parameter rotates clockwise by  $90^\circ$  in the first step and then rotates back to its original orientation in the second step. In each step, the  $X_2^+$  order parameter turns off so it reaches zero at the  $Cm2a$  structure and then turns on again reoriented by  $90^\circ$ . The  $Cm2a$  structure is shown in Fig. 3(b). Here the  $(a, a)$  direction of  $X_3^+$  establishes an octahedral tilt pattern where the tilt axes of adjacent perovskite layers are perpendicular to each other, so there are  $a^-b^0b^0$  and  $b^0a^-b^0$  rotations in the dark and light grey perovskite layers in Fig. 3(b), respectively. Note that the higher energy  $Cm2m$  pathway follows a similar evolution of structural order parameters as the  $Cm2a$  path, except the  $X_2^+$  rather than the  $X_3^+$  order parameter rotates during the switching process.

The second two-step switching path that we investigate is shown in Fig. 2(c). The  $\Gamma_5^-$  and  $X_3^+$  order parameters follow the same sequence as in Fig. 2(b), except now the  $X_2^+$  order parameter makes two  $90^\circ$  rotations while maintaining finite amplitude, rather than turning off/on. The barrier structure in

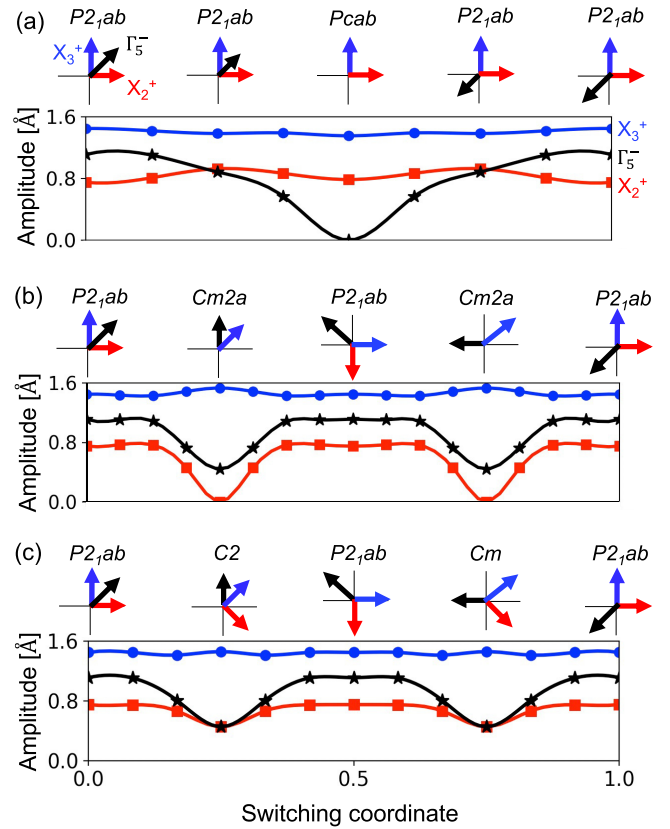


FIG. 4. Amplitudes of the  $X_3^+$ ,  $X_2^+$ , and  $\Gamma_5^-$  structural distortions as a function of switching coordinate for each of the switching paths shown in Fig. 2: (a) one-step switching with barrier  $Pcab$ , (b) two-step switching with barrier  $Cm2a$ , and (c) two-step switching with barriers  $C2/Cm$ . The amplitudes are obtained from NEB calculations and are reported for a 36-atom computational cell.

the first step has symmetry  $C2$ , whereas in the second step it has symmetry  $Cm$ . The  $C2$  and  $Cm$  structures are shown in Figs. 3(c) and 3(d), respectively. These structures have the same  $a^-b^0b^0/b^0a^-b^0$  octahedral tilt pattern as  $Cm2a$ . The  $C2$  and  $Cm$  structures share the same  $X_2^+$  rotation pattern, where every other perovskite layer [those colored green in Figs. 3(c) and 3(d)] exhibit finite amplitude rotations about  $[0\ 0\ 1]$  and the other (grey) layers have no  $X_2^+$  rotation amplitude. The difference between the  $C2$  and  $Cm$  structures is the orientation of the polarization with respect to the  $X_3^+$  and  $X_2^+$  order parameters: In  $C2$  the polarization lies along the  $X_3^+$  tilt axis of the green octahedra which have finite  $X_2^+$  rotations, whereas in  $Cm$  the polarization lies along the  $X_3^+$  tilt axis of the grey octahedra which have no  $X_2^+$  rotation.

To investigate how the energy changes during switching, Fig. 2(d) shows NEB calculations of the energy as a function of switching coordinate for the paths in Figs. 2(a)–2(c). Both two-step paths have a significantly lower energy barrier than the one-step  $Pcab$  path, with the energy barriers for the  $C2/Cm$  path (96.68 and 99.06 meV/f.u. in the first and second steps, taken from Table II) being slightly lower than the  $Cm2a$  path (103.46 meV/f.u.).

Figure 4 shows how the amplitudes of the  $X_3^+$ ,  $X_2^+$ , and polar  $\Gamma_5^-$  distortions evolve along each ferroelectric switching path, obtained from NEB calculations. In the one-step

switching path shown in Fig. 4(a), the polar distortion amplitude goes to zero at the barrier structure  $Pcab$ , whereas the  $X_2^+$  and  $X_3^+$  distortion amplitudes remain almost unchanged throughout the switching process. In the two-step switching path via  $Cm2a$  shown in Fig. 4(b), at the  $Cm2a$  barrier the polar distortion amplitude decreases by about half and that of  $X_2^+$  amplitude goes to zero, whereas the  $X_3^+$  amplitude again changes very little throughout the switching process. Finally, for the two-step  $C2/Cm$  path shown in Fig. 4(c), all three distortion amplitudes remain finite throughout the switching process, although the polar and  $X_2^+$  amplitudes are suppressed upon approaching the  $C2/Cm$  barriers.

To summarize, we find that the two-step switching paths have lower energy barriers than the one-step switching path in  $\text{Bi}_2\text{WO}_6$ . This implies that switching proceeds via two  $90^\circ$  steps, in agreement with the experimental observations of Ref. [29]. We find that the two-step paths that pass through  $C2/Cm$  and  $Cm2a$  have almost the same energy barrier ( $\approx 100$  meV/f.u.), with the barrier for the  $C2/Cm$  path being slightly lower. We also investigate the epitaxial strain dependence of these energy barriers (Appendix B) and find that the two-step barriers remain the lowest energy except possibly under highly compressive strains. The two-dimensional structural order parameters facilitate the lower energy two-step switching, which involves order parameter rotation rather than completely turning the polarization off/on. We make use of these ferroelectric switching paths in the next section to guide us to the relevant structural phases in which to explore the spin orientation of magnetic dopants in  $\text{Bi}_2\text{WO}_6$ .

### C. Spin directionality of magnetic dopants

We next investigate the impact of polarization reversal on the spin orientation of magnetic dopants in  $\text{Bi}_2\text{WO}_6$ . Magnetic dopants in  $\text{Bi}_2\text{WO}_6$  exhibit magnetocrystalline anisotropy—a preferred directionality of the unpaired electron spins—that arises due to the crystal field at the dopant site and spin-orbit coupling. Here, we consider  $\text{Fe}^{3+}$  substitutional defects on W sites, which is one of the potential defect species in  $\text{Bi}_2\text{WO}_6$ . Although the  $P2_1ab$  structure only contains one distinct W site, the barrier structures encountered in the two-step switching processes contain multiple symmetry-distinct W sites (and hence dopant positions), which are shown in Figs. 3(b)–3(d). The energetics of this defect and alternative Fe sites will be fully considered in a forthcoming work.

Figure 5 tracks the change in the MCAE surface along the two lowest energy-switching pathways,  $P2_1ab \rightarrow C2 \rightarrow P2_1ab$  and  $P2_1ab \rightarrow Cm \rightarrow P2_1ab$  and  $P2_1ab \rightarrow Cm2a \rightarrow P2_1ab$ , revealing the change in directionality of the Fe-dopant spins during switching. Beginning in the  $P2_1ab$  phase with the polarization  $\mathbf{P}$  oriented along  $[1\ 0\ 0]$ , we identify a spin easy axis that lies in the crystallographic  $ab$  plane at  $11^\circ$  with respect to  $\mathbf{P}$ . In the octahedral orientation indicated in the first step, the spin easy axis is along  $\langle 1.0, -0.2, 0.0 \rangle$ . The calculated magnitude of the MCAE is  $530\ \mu\text{eV}$ , which is the energy difference between the  $x$  and  $z$  principal axes of the MCAE surface. In addition, we calculate an in-plane anisotropy between the  $x$  and  $y$  principal axes of  $130\ \mu\text{eV}$ . The principal axes of the

TABLE III.  $\text{Fe}^{3+}$  dopant positions, site symmetries, and MCAEs in  $P2_1ab$  and intermediate switching phases. \* indicates the site chosen for the switching pathway in Fig. 5(b), where multiple sites are available.

Phase	Wyckoff site	Site symmetry	MCAE ( $\mu\text{eV}$ )	
			Out of plane	In plane
$P2_1ab$	4a	1	530	130
$Cm2a$	4b	2	730	210
	4c	$m$	940	510
	2a*	$m$	970	520
$Cm$	2a	$m$	980	530
	4b	1	650	130
	2b*	2	750	210
$C2$	2b	2	760	200
	4c	1	N/A	

MCAE surface for each of the switching steps are given in Appendix C.

Taking the  $Cm2a$  path [Fig. 5(a)], the Fe dopant (along with all the octahedra in the top layer) first passes through the 4c Wyckoff position in  $Cm2a$ , which has site symmetry  $m$ . On this site, the MCAE is significantly increased to  $940\ \mu\text{eV}$  and the spin easy axis is  $\langle -0.7, 0.7, 0.0 \rangle$ . At  $90^\circ$  switching, the structure returns to the  $P2_1ab$  phase with spin easy axis now along  $\langle -0.2, 1.0, 0.0 \rangle$ , a rotation of  $112^\circ$  around the  $c$  axis from the original spin easy axis. Passing through the  $Cm2a$  structure a second time, the dopant (and all octahedra in the top layer) is in the 4b Wyckoff position with site-symmetry 2, resulting in a slightly lower MCAE of  $730\ \mu\text{eV}$  compared to the 4c site, although the spin easy axis remains the same. This can be understood by the variation in off-centering of Fe, making a  $170^\circ$  O–Fe–O bond angle in the 4c position compared to  $180^\circ$  in the 4b position (taking the bonds aligned parallel to the spin axis). In the last step, the structure returns to  $P2_1ab$  with  $\mathbf{P}$  switched by  $180^\circ$  and the spin easy axis returned to  $\langle 1.0, -0.2, 0.0 \rangle$ . (Beginning in one of the positions in the lower layer, the Fe dopant would pass through the 4b Wyckoff position first and the 4c position second.)

Alternatively, taking the  $C2/Cm$  path [Fig. 5(b)], the Fe dopant first passes through the  $C2$  phase in Wyckoff position 2b (site-symmetry 2) and secondly through the  $Cm$  phase in Wyckoff position 2a (site symmetry  $m$ ). The MCAE values are  $750\ \mu\text{eV}$  and  $970\ \mu\text{eV}$ , respectively, and the spin easy axis is along  $\langle -0.7, 0.7, 0.0 \rangle$  in both cases. As in the  $Cm2a$  path, a  $90^\circ$  switch in the polarization direction results in a rotation of the spin easy axis by  $112^\circ$  about the  $c$  axis. The similarity in crystal field environment in the two switching pathways accounts for the resemblance between the MCAE surfaces in Figs. 5(a) and 5(b). Details of the site symmetries and in-plane and out-of-plane MCAEs are listed in Table III, including alternative dopant positions. There are symmetrically inequivalent W sites on the 2a Wyckoff position in  $Cm$  and the 2b position in  $C2$ , which have a slightly different crystal field environment from the sites considered above, resulting in small differences in the MCAE values. In addition, an alternative domain choice for the switching pathways

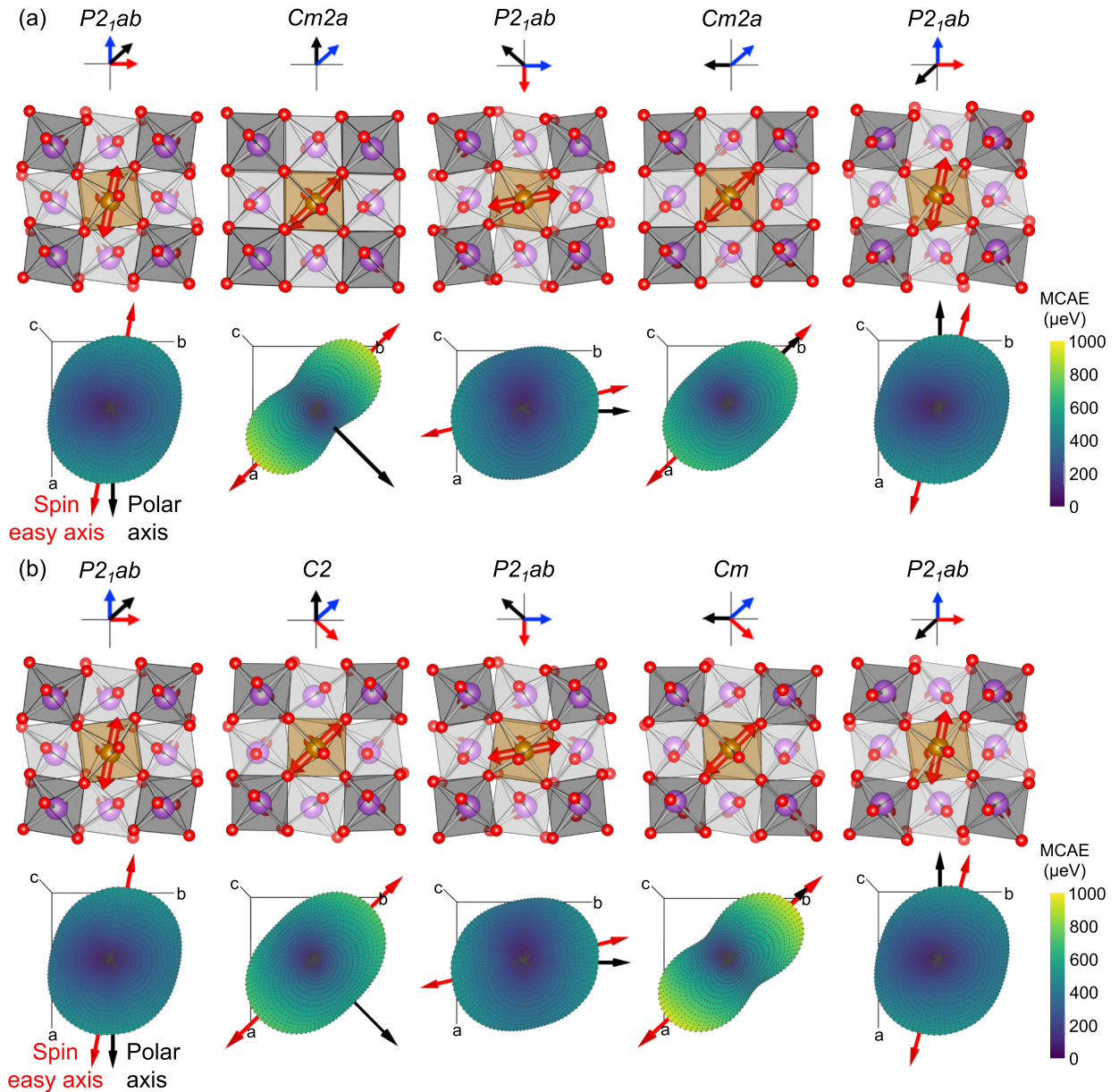


FIG. 5. Change in spin directionality on an Fe dopant during switching (a) via the  $Cm2a$  intermediate phase and (b) via the  $C2$  and  $Cm$  phases. Magnetocrystalline anisotropy energy surfaces are plotted with red arrows indicating the spin easy directions and black arrows showing the polar axis in the  $P2_1ab$  phases. In the crystal structures, purple, red, and gold spheres are W, O, and Fe, respectively, and only WO<sub>6</sub> octahedra are shown; the Fe dopant sits in the upper layer with the dark grey octahedra and the lower layer is light grey.

could have taken the Fe dopant through the  $4b$  position in  $Cm$  and the  $4c$  position in  $C2$ . MCAE data is not available for the latter as the structural optimization on this site did not converge the forces on the ions below a reasonable number.

The MCAEs reported here are typical of  $3d$  transition metal atoms [48,49] and their low magnitudes indicate that thermally induced switching could occur if not kept at very low temperatures. This could be sufficient for devices operating at cryogenic temperatures (e.g., quantum computing); an MCAE of 0.5 meV corresponds to an energy barrier of  $\sim 6$  K, three orders of magnitude greater than the typical

mK operating temperatures of many quantum devices. However, strategies to increase the MCAE should be explored to exclude thermally induced switching in higher temperature applications. These could include systems with reduced dimensionalities and  $4d$  or  $5d$  transition metal and rare earth atoms which have been shown to exhibit giant MCAE values [50–53].

#### IV. CONCLUSION

We use a combination of group theoretic analysis and DFT calculations to determine the intrinsic ferroelectric switching



TABLE IV. Subgroups of  $I4/mmm$  established by distinct directions of the  $\Gamma_5^-$ ,  $X_2^+$ , and  $X_3^+$  order parameters. Total energies, distortion amplitudes, and lattice parameters obtained from DFT structural relaxations of  $\text{Bi}_2\text{WO}_6$  in each space group are given. The energies are reported relative to the energy of  $P2_1ab$ , which is set to 0 meV/f.u., and the distortion amplitudes are obtained by decomposing the distorted structures with respect to  $I4/mmm$  and are reported for a 36-atom computational cell.

Irrep	Direction	Space group ( $N^\circ$ )	Amplitude ( $\text{\AA}$ )	Lattice parameters ( $\text{\AA}$ )			Energy (meV/f.u.)
				$a$	$b$	$c$	
$\Gamma_5^-$	$(a, 0)$	$Imm2$ (44)	1.47	5.472	5.472	16.575	154.54
	$(a, a)$	$Fmm2$ (42)	1.25	5.504	5.461	16.436	133.91
$X_2^+$	$(a, 0)$	$Bbcm$ (64)	1.31	5.290	5.290	16.646	231.32
	$(a, a)$	$P4/mbm$ (127)	0.80	5.349	5.349	16.524	310.16
$X_3^+$	$(a, 0)$	$Bbcm$ (64)	1.48	5.368	5.395	16.663	178.40
	$(a, a)$	$P4_2/ncm$ (138)	1.51	5.393	5.393	16.576	161.40

pathways of  $\text{Bi}_2\text{WO}_6$ . We identify several pathways: a one-step pathway, via  $Pcab$ , and three two-step pathways, via  $C2/Cm$ ,  $Cm2a$ , and  $Cm2m$ . By comparing energies of the barrier structures, we find that the two-step paths are lower energy than the one-step path, in agreement with experiments [29]; in particular, the  $C2/Cm$  path provides the lowest energy barrier of 97-99 meV/f.u. and the  $Cm2a$  barrier is only slightly higher at 103 meV/f.u.. These intrinsic switching barrier energies are comparable to those of other structurally complex ferroelectrics such as  $\text{LiNbO}_3$  and  $\text{Ca}_3\text{Ti}_2\text{O}_7$ , which have barriers of 130 meV/f.u. [54] and 64 meV/f.u. [34], respectively.

Magnetic defects experience a change in crystal field environment during switching, resulting in a change in magnetic anisotropy at each switching step. Contrasting with  $\text{Fe}^{3+}$  dopants in  $\text{PbTiO}_3$  which exhibit a spin easy plane [10], the lower crystallographic symmetry of  $\text{Bi}_2\text{WO}_6$  results in a spin easy axis. By calculating MCAE surfaces, we find how the spin orientation of a  $\text{Fe}^{3+}$  substitutional defect on W sites changes during polarization switching. In the  $P2_1ab$  structure, the spin easy axis is in the  $ab$  plane at  $11^\circ$  with respect to the polar axis and has an out-of-plane MCAE of  $530 \mu\text{eV}$  and an in-plane MCAE of  $130 \mu\text{eV}$ . During ferroelectric switching via intermediate phases, the spin easy axis rotates within the  $ab$  plane and the MCAE is considerably increased ( $650\text{--}980 \mu\text{eV}$  out of plane,  $130\text{--}530 \mu\text{eV}$  in plane) due to changes in the local crystal environment of the dopant. We

find that switching the polarization by  $90^\circ$  in  $\text{Bi}_2\text{WO}_6$  results in a  $112^\circ$  rotation of the spin easy axis. However, a full  $180^\circ$  reversal of the polarization returns the spin easy axis to its original orientation.

Based on these results, we suggest that a possible pathway to achieve full spin control with  $180^\circ$  polarization switching is to consider ferroelectrics where an additional structural distortion that couples to the polarization must change during  $180^\circ$  switching. If this structural distortion also impacts the magnetic anisotropy, then the change to the distortion due to polarization switching may result in a different spin easy axis in the  $+P$  and  $-P$  states. For example, changes to octahedral rotation distortions, which are extremely common in (layered) perovskite oxides, can modify spin easy planes and axes [55,56]. Although the  $X_3^+$  and  $X_2^+$  octahedral rotation patterns in  $\text{Bi}_2\text{WO}_6$  change along the two-step switching paths, the octahedral rotation amplitudes and pattern in the starting ( $+P$ ) and final ( $-P$ ) structures are the same. However, there are other layered perovskite ferroelectrics, such as the Aurivillius compound  $\text{SrBi}_2\text{Ta}_2\text{O}_9$  [57] and several  $n=2$  Ruddlesden-Popper ferroelectric oxides [34,58], where reversal of the polarization requires *by symmetry* that the sense of an octahedral rotation is also reverse. Compounds such as these may provide the necessary ingredients to create distinct low-symmetry environments and hence different MCAE surfaces in polarization reversed states.

TABLE V. Principal axes of the MCAE surfaces for each of the switching steps shown in Fig. 5.

Switching figure	Phase	Wyckoff site	Principal axes		
			$x$	$y$	$z$
5(a)	$P2_1ab$	$4a$	[1.0-0.2 0.0]	[0.2 0.9 0.3]	[-0.1-0.3 0.9]
	$Cm2a$	$4c$	[0.7-0.7 0.0]	[0.6 0.6-0.5]	[-0.3-0.3-0.9]
	$P2_1ab$	$4a$	[-0.2 1.0 0.0]	[-0.9-0.2-0.3]	[-0.3-0.1 0.9]
	$Cm2a$	$4b$	[0.7-0.7 0.0]	[-0.7-0.7-0.3]	[0.2 0.2-0.9]
	$P2_1ab$	$4a$	[-1.0 0.2 0.0]	[0.2 0.9 0.3]	[0.1 0.3-0.9]
5(b)	$P2_1ab$	$4a$	[1.0-0.2 0.0]	[0.2 0.9 0.3]	[-0.1-0.3 0.9]
	$C2$	$2b$	[0.7-0.7 0.0]	[-0.7-0.7-0.3]	[0.2 0.2-1.0]
	$P2_1ab$	$4a$	[-0.2 1.0 0.0]	[-0.9-0.2-0.3]	[-0.3-0.1 0.9]
	$Cm$	$2a$	[-0.7 0.7 0.0]	[-0.6-0.6-0.4]	[-0.3-0.3 0.9]
	$P2_1ab$	$4a$	[-1.0 0.2 0.0]	[0.2 0.9 0.3]	[0.1 0.3-0.9]



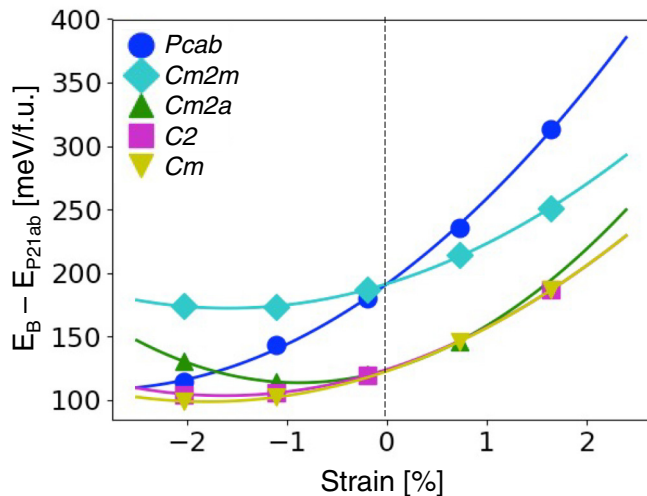


FIG. 6. Energy of the ferroelectric switching barrier structures ( $E_B$ ) above  $P2_{1ab}$  as a function of epitaxial strain. The strain is applied biaxially in the  $ab$  plane and 0% strain is defined with respect to the  $P2_{1ab}$  lattice parameters.

#### ACKNOWLEDGMENTS

This paper was supported by the Microelectronics Co-Design Research Program, under the Office of Science of the U.S. Department of Energy under Contract No. DE-AC02-05CH11231 (K.I., N.L., and S.M.G.). N.P., Z.C., S.P.R., and E.A.N. acknowledge support from University of California, Merced. Computational resources were provided by the National Energy Research Scientific Computing Center and the Molecular Foundry, DOE Office of Science User Facilities supported by the Office of Science, U.S. Department of Energy under Contract No. DE-AC02-05CH11231. The work performed at the Molecular Foundry was supported by the Office of Science, Office of Basic Energy Sciences, of the U.S. Department of Energy under the same contract. We also acknowledge the use of computational resources supported by the Center for Functional Nanomaterials, which is a U.S. DOE Office of Science Facility, and the Scientific Data and Computing Center, a component of the Computational Science

Initiative, at Brookhaven National Laboratory under Contract No. DE-SC0012704. In addition, this work used the Extreme Science and Engineering Discovery Environment (XSEDE) Expanse cluster at the San Diego Supercomputing Center through allocation TG-PHY200085.

K.I. and N.P. contributed equally to this work.

#### APPENDIX A: ADDITIONAL SUBGROUPS OF $I4/mmm$

Table IV reports the subgroups of  $I4/mmm$  generated by distinct directions of the  $\Gamma_5^-$ ,  $X_2^+$ , and  $X_3^+$  order parameters, along with the distortion amplitudes, lattice parameters, and total energies of  $\text{Bi}_2\text{WO}_6$  after DFT structural relaxations in each space group.

#### APPENDIX B: EPITAXIAL STRAIN

Figure 6 presents the energies of the ferroelectric switching barrier structures discussed in the main text as a function of epitaxial strain. In these calculations, biaxial strain is applied in the  $ab$  plane, and the lattice parameter  $c$  and all atomic positions are allowed to relax. We find that all energy barriers increase upon going from compressive to tensile strain. The  $Pcab$  energy barrier changes the most dramatically with strain. The  $C2/Cm$  structures provide the lowest energy barriers at all strains that we consider, although under highly compressive strains (larger than 2%) the  $Pcab$  barrier may become lowest, which would suggest a crossover from two- to one-step switching being the lowest energy path.

#### APPENDIX C: PRINCIPAL AXES OF MAGNETOCRYSTALLINE ANISOTROPY ENERGY SURFACES

Table V reports the principal axes of the MCAE surfaces shown in Fig. 5. These axes are orthonormal vectors which describe the three principal axes of rotation of the MCAE surface. The spin easy axis lies along the  $x$  principal axis.

- [1] N. A. Spaldin and R. Ramesh, *Nat. Mater.* **18**, 203 (2019).
- [2] S. Manipatruni, D. E. Nikonov, C. C. Lin, T. A. Gosavi, H. Liu, B. Prasad, Y. L. Huang, E. Bonturim, R. Ramesh, and I. A. Young, *Nature (London)* **565**, 35 (2019).
- [3] J. A. Mundy, C. M. Brooks, M. E. Holtz, J. A. Moyer, H. Das, A. F. Rébola, J. T. Heron, J. D. Clarkson, S. M. Disseler, Z. Liu, A. Farhan, R. Held, R. Hovden, E. Padgett, Q. Mao, H. Paik, R. Misra, L. F. Kourkoutis, E. Arenholz, A. Scholl, J. A. Borchers, W. D. Ratcliff, R. Ramesh, C. J. Fennie, P. Schiffer, D. A. Muller, and D. G. Schlom, *Nature (London)* **537**, 523 (2016).
- [4] R. Cai, V.-A. Antohe, Z. Hu, B. Nysten, L. Piraux, and A. M. Jonas, *Adv. Mater.* **29**, 1604604 (2017).
- [5] G. Catalan, J. Seidel, R. Ramesh, and J. F. Scott, *Rev. Mod. Phys.* **84**, 119 (2012).
- [6] J. Wang, J. B. Neaton, H. Zheng, V. Nagarajan, S. B. Ogale, B. Liu, D. Viehland, V. Vaithyanathan, D. G. Schlom, U. V. Waghmare, N. A. Spaldin, K. M. Rabe, M. Wuttig, and R. Ramesh, *Science* **299**, 1719 (2003).
- [7] A. K. Boudalis, J. Robert, and P. Turek, *Chem. Eur. J.* **24**, 14896 (2018).
- [8] J. Liu, J. Mrozek, W. K. Myers, G. A. Timco, R. E. P. Winpenny, B. Kintzel, W. Plass, and A. Ardavan, *Phys. Rev. Lett.* **122**, 037202 (2019).
- [9] M. Fittipaldi, A. Cini, G. Annino, A. Vindigni, A. Caneschi, and R. Sessoli, *Nat. Mater.* **18**, 329 (2019).
- [10] J. Liu, V. V. Laguta, K. Inzani, W. Huang, S. Das, R. Chatterjee, E. Sheridan, S. M. Griffin, A. Ardavan, and R. Ramesh, *Sci. Adv.* **7**, eabf8103 (2021).

- [11] A. I. Johnson, F. Islam, C. M. Canali, and M. R. Pederson, *J. Chem. Phys.* **151**, 174105 (2019).
- [12] V. I. Utkin, Y. E. Roginskaya, V. I. Voronkova, V. K. Yanovskii, B. Sh. Galyamov, and Y. N. Venevtsev, *Phys. Stat. Sol. (a)* **59**, 75 (1980).
- [13] T. Jardiel, A. C. Caballero, and M. Villegas, *J. Ceram. Soc. Jpn.* **116**, 511 (2008).
- [14] M. Campanini, M. Trassin, C. Ederer, R. Erni, and M. D. Rossell, *ACS Appl. Elect. Mater.* **1**, 1019 (2019).
- [15] C.-P. De Araujo, J. Cuchiaro, L. McMillan, M. Scott, and J. Scott, *Nature (London)* **374**, 627 (1995).
- [16] X. Mao, W. Wang, X. Chen, and Y. Lu, *Appl. Phys. Lett.* **95**, 013704 (2009).
- [17] L. Keeney, T. Maity, M. Schmidt, A. Amann, N. Deepak, N. Petkov, S. Roy, M. E. Pemble, and R. W. Whatmore, *J. Am. Ceram. Soc.* **96**, 2339 (2013).
- [18] X. Chen, J. Xiao, Y. Xue, X. Zeng, F. Yang, and P. Su, *Cera. Int.* **40**, 2635 (2014).
- [19] J. Wang, Z. Fu, R. Peng, M. Liu, S. Sun, H. Huang, L. Li, R. J. Knize, and Y. Lu, *Mater. Horiz.* **2**, 232 (2015).
- [20] Z. Li, J. Ma, Z. Gao, G. Viola, V. Koval, A. Mahajan, X. Li, C. Jia, C. Nan, and H. Yan, *Dalton Trans.* **45**, 14049 (2016).
- [21] L. Keeney, S. Kulkarni, N. Deepak, M. Schmidt, N. Petkov, P. F. Zhang, S. Cavill, S. Roy, M. E. Pemble, and R. W. Whatmore, *J. Appl. Phys.* **112**, 052010 (2012).
- [22] K. Moore, E. N. O'Connell, S. M. Griffin, C. Downing, L. Colfer, M. Schmidt, V. Nicolosi, U. Bangert, L. Keeney, and M. Conroy, *ACS Appl. Mater. Interfaces* **14**, 5525 (2022).
- [23] A. Y. Birenbaum and C. Ederer, *Phys. Rev. B* **90**, 214109 (2014).
- [24] X. Zhai, A. J. Grutter, Y. Yun, Z. Cui, and Y. Lu, *Phys. Rev. Materials* **2**, 044405 (2018).
- [25] A. Faraz, T. Maity, M. Schmidt, N. Deepak, S. Roy, M. E. Pemble, R. W. Whatmore, and L. Keeney, *J. Amer. Ceram. Soc.* **100**, 975 (2017).
- [26] R. Machado, M. G. Stachiotti, R. L. Migoni, and A. H. Tera, *Phys. Rev. B* **70**, 214112 (2004).
- [27] C. E. Mohn and S. Stølen, *Phys. Rev. B* **83**, 014103 (2011).
- [28] H. Djani, E. Bousquet, A. Kellou, and P. Ghosez, *Phys. Rev. B* **86**, 054107 (2012).
- [29] C. Wang, X. Ke, J. J. Wang, R. Liang, Z. Luo, Y. Tian, D. Yi, Q. Zhang, J. J. Wang, X. F. Han, G. Van Tendeloo, L. Q. Chen, C. W. Nan, R. Ramesh, and J. Zhang, *Nat. Commun.* **7**, 10636 (2016).
- [30] H. Okudera, Y. Sakai, K. Yamagata, and H. Takeda, *Acta Crystallogr. Sec. B* **74**, 295 (2018).
- [31] N. A. McDowell, K. S. Knight, and P. Lightfoot, *Chem. Eur. J.* **12**, 1493 (2006).
- [32] S. P. Beckman, X. Wang, K. M. Rabe, and D. Vanderbilt, *Phys. Rev. B* **79**, 144124 (2009).
- [33] J. Heron, J. Bosse, Q. He, Y. Gao, M. Trassin, L. Ye, J. Clarkson, C. Wang, J. Liu, S. Salahuddin *et al.*, *Nature (London)* **516**, 370 (2014).
- [34] E. A. Nowadnick and C. J. Fennie, *Phys. Rev. B* **94**, 104105 (2016).
- [35] G. Kresse and J. Hafner, *Phys. Rev. B* **47**, 558 (1993).
- [36] G. Kresse and J. Hafner, *Phys. Rev. B* **49**, 14251 (1994).
- [37] G. Kresse and J. Furthmüller, *Comp. Mater. Sci.* **6**, 15 (1996).
- [38] G. Kresse and J. Furthmüller, *Phys. Rev. B* **54**, 11169 (1996).
- [39] P. E. Blöchl, *Phys. Rev. B* **50**, 17953 (1994).
- [40] G. Kresse and D. Joubert, *Phys. Rev. B* **59**, 1758 (1999).
- [41] J. P. Perdew, A. Ruzsinszky, G. I. Csonka, O. A. Vydrov, G. E. Scuseria, L. A. Constantin, X. Zhou, and K. Burke, *Phys. Rev. Lett.* **100**, 136406 (2008).
- [42] G. Henkelman, B. P. Uberuaga, and H. Jónsson, *J. Chem. Phys.* **113**, 9901 (2000).
- [43] S. L. Dudarev, G. A. Botton, S. Y. Savrasov, C. J. Humphreys, and A. P. Sutton, *Phys. Rev. B* **57**, 1505 (1998).
- [44] H. Stokes, D. Hatch, and B. Campbell. ISOTROPY software suite, <http://stokes.byu.edu/isotropy.html>.
- [45] K. Momma and F. Izumi, *J. Appl. Crystallogr.* **41**, 653 (2008).
- [46] A. Glazer, *Acta Crystallogr. Sec. B* **28**, 3384 (1972).
- [47] A. D. Rae, J. G. Thompson, and R. L. Withers, *Acta Crystallogr. Sec. B* **47**, 870 (1991).
- [48] A. Schrön, C. Rödl, and F. Bechstedt, *Phys. Rev. B* **86**, 115134 (2012).
- [49] I. G. Rau, S. Baumann, S. Rusponi, F. Donati, S. Stepanow, L. Gagnaniello, J. Dreiser, C. Piamonteze, F. Nolting, S. Gangopadhyay *et al.*, *Science* **344**, 988 (2014).
- [50] J.-X. Yu and J. Zang, *Sci. Adv.* **4**, eaar7814 (2018).
- [51] M. Ležaić and N. A. Spaldin, *Phys. Rev. B* **83**, 024410 (2011).
- [52] P. C. Rout and U. Schwingenschlögl, *Nano Lett.* **21**, 6807 (2021).
- [53] J. Zhou, Q. Wang, Q. Sun, Y. Kawazoe, and P. Jena, *Phys. Chem. Chem. Phys.* **17**, 17182 (2015).
- [54] M. Ye and D. Vanderbilt, *Phys. Rev. B* **93**, 134303 (2016).
- [55] Z. Liao, M. Huijben, Z. Zhong, N. Gauquelin, S. Macke, R. Green, S. Van Aert, J. Verbeeck, G. Van Tendeloo, K. Held *et al.*, *Nat. Mater.* **15**, 425 (2016).
- [56] D. Yi, C. L. Flint, P. P. Balakrishnan, K. Mahalingam, B. Urwin, A. Vailionis, A. T. NDiaye, P. Shafer, E. Arenholz, Y. Choi, K. H. Stone, J. H. Chu, B. M. Howe, J. Liu, I. R. Fisher, and Y. Suzuki, *Phys. Rev. Lett.* **119**, 077201 (2017).
- [57] J. M. Perez-Mato, M. Aroyo, A. García, P. Blaha, K. Schwarz, J. Schweifer, and K. Parlinski, *Phys. Rev. B* **70**, 214111 (2004).
- [58] N. A. Benedek and C. J. Fennie, *Phys. Rev. Lett.* **106**, 107204 (2011).